Draft version November 26, 2012
Preprint typeset using LaTeX style emulateapj v. 11/10/09

HIGH RESOLUTION HST-COS Lyα PROFILE

C. Scarlata, J. Colbert, H. I. Teplitz
Spitzer Science Center, California Institute of Technology, 314-6, Pasadena, CA-91125

N. Panagia[2,7,9], M. Hayes[3], B. Siana[4], A. Rau[4,5], P. Francis[6], A. Caon[1,8], A. Pizzella[8], C. Bridge[1]

Draft version November 26, 2012

ABSTRACT

Subject headings: galaxies: ISM — ISM: structure

1. INTRODUCTION

We use a standard $H_0 = 70$ km s^{-1} Mpc^{-1}, $\Omega_M = 0.3$, and $\Omega_\Lambda = 0.7$ cosmology.

2. THE SAMPLE

The targets for the HST COS spectroscopic followup are taken from the sample of Lyα emitters identified by Deharveng et al. (2008) and Cowie et al. (2010) in deep GALEX grism spectroscopy. The GALEX sample includes 119 Lyα emitters, 49 of which have rest-frame Lyα emission line EW > 20Å. From the parent sample of GALEX Lyα emitters, we originally selected 25 galaxies that satisfied the following criteria: 1) are classified as star-forming based on optical emission line ratios (e.g., Cowie et al. 2010), 2) have Lyα emission line rest–frame EW> 20 Å in the low resolution GALEX spectra, and 3) have redshift confirmed using optical spectroscopy. As we show in Scarlata et al. (2009), Atek et al. (2009), Finkelstein et al. (2009), and Cowie et al. (2010), the requirement of having the optical confirmation does not change the target selection function of the sample, since 100% of the sources we followed up were, in fact, confirmed. High redshift Lyα emitters are usually selected with Hu et al.'s (1998) definition that they have a rest frame EW greater than 20 Å (see also Kornei et al. 2010). Thus, the EW cut ensures that we are able to make a valid comparison with the samples of Lyα emitters selected at $z > 2$.

Deharveng et al. (2008) identified broad-line AGN in their sample of Lyα emitters as those objects with Lyα line widths broader than 1200 km s^{-1}. Narrow line AGN could not be identified since other diagnostic lines of AGN activity were either too faint, or fell in a noisy part of the UV spectra. In order to identify the narrow line AGN, we have used the classic Baldwin et al. (1981, BPT) diagram of [O III]/Hβ versus [N II]/Hα(shown in Figure **??**).

3. OBSERVATIONS AND DATA ANALYSIS

The galaxies were observed between February and October 2011, with the COS FUV, medium-resolution G160 grism. Each galaxy was observed for 1 orbit. For 22 out of the 25 galaxies, the imaging target acquisition was performed on a star close to the science target (distance $\leq$ 2'). The telescope was then offset to center the COS aperture on the science target. The offsets were computed from ground based images in most cases, while ACS HST imaging was used for the objects in the COSMOS field (see Table **??**). In order to check the acquisition procedure, we obtained a direct NUV image after the telescope was shifted to te target position. The exposure times of the images vary between 80 and 200 seconds, depending on the GALEX NUV magnitude of the target. The remaining of each orbit was used for the spectroscopic observations in TIME-TAG mode, with typical exposure times of 2300s. We chose the grism central wavelength to ensure that the Lyα would not fall in the wavelength gaps due to the physical layout of the detectors and the optics. In order to minimize the impact of microchannel plate detector fixed pattern noise, we took two exposures for each target, with FP-POS= 3 and FP-POS= 4, respectively. The wavelength range covered by the COS spectra is approximately $1405 - 1775$Å, with a dispersion of 12.23Å px^{-1}.

We recalibrated and re-extracted the COS spectra using `calcos` v2.15.4 task in pyraf. Due to the target acquisition strategy, the galaxies were not perfectly centered in the COS aperture. We used the direct NUV images to measure the shifts in the dispersion direction between the position of the center of each galaxy and the expected position of the COS aperture center. The shifts ranged between -19 and 10 NUV pixels, with a standard deviation of 8 pixels (corresponding to 0.1Å). The correction to the wavelength zero point was applied to the wavelength column in the `corrtag` files, and `calcos` was the run again with the edited files as input. This correction does not only take care of the wavelength zero point, but also allows us to apply the proper sensitivity at each wavelength.

The PSA aperture throughput decreases toward the edges of the field of view, due to the increasing vignetting of the flux. This change in throughput is not accounted

[2] Space Telescope Science Institute, 3700 San Martin Drive, Baltimore, MD 21218, USA
[3] Observatoire de Geneve, 51, Ch. des Maillettes, CH-1290, Sauverny, Switzerland
[4] California Institute of Technology, MS 105-24, Pasadena, CA91125
[5] Max-Planck-Institut für extraterrestrische Physik, Giessenbachstrasse 1, 85748 Garching, Germany
[6] Research School of Astronomy and Astrophysics, the Australian National University, Canberra 0200, Australia
[7] INAF/Osservatorio Astrofisico di Catania, Via S.Sofia 78, I-95123 Catania, Italy
[8] Department of Astronomy, University of Padova, Vicolo dell'Osservatorio 3, I-35122, Padova, Italy
[9] Supernova Ltd., Olde Yard Village 131, Northsound Road, Virgin Gorda, British Virgin Islands

for in the `calcos` pipeline, resulting in an underestimate of the extracted flux for extended sources. We scaled the extracted spectra by a correction factor computed using the directing imaging, and assuming that the aperture throughput is symmetric with respect to the aperture center. The scaling factors vary between 1.15 and 1.45, for the most compact and most extended sources, respectively. In Figure **??** we compare the total aperture corrected NUV flux measured from the COS images within the 2.″5 aperture with the GALEX NUV total flux. The fluxes in the smaller COS apertures are systematically lower than the GALEX fluxes, indicating that

For four galaxies (see Table **??**) the star used for the acquisition was too bright to be observed with MIRRORA. We then performed the acquisition using MIRRORB and moved to MIRRORA for the science exposures. Although the change from MIRRORB to MIRRORA does not affect a targets relative location to the aperture, it does move the apertures location on the detector, making it impossible to measure the precise target's location in the aperture, even if a direct image was obtained after the shift. Because the zero point of the wavelength calibration depends on the position of the galaxy in the aperture, for these four galaxies we added a systematic error component to the wavelength calibration, equal to the standard deviation of the galaxies' centers in the dispersion direction (0.1Å, c.f.t. above).

3.1. *Measurement of line flux and wavelength of line peak*

We show the Lyα profiles of the sample galaxies in Figure **??**. The profiles are characterized by complex structure and asymmetric shape. For this reason, rather than fitting a single gaussian, we measure the total line flux by integrating the profile between $\pm$2.5Å from the expected line center. We estimate the continuum by computing the median flux density within 2Å on both sides of the line center. The line-flux error was computed from the error spectrum derived during the spectral extraction process. In Figure **??** we compare the total, aperture–corrected Lyα flux from the COS spectra, with the line intensity derived in **?**. The aperture–correction was estimated using the acquisition images, as explained in Section 3. The comparison between the GALEX and COS measurements is informative, because the two instruments have different aperture size.

For each galaxy, we also derived the wavelength corresponding to the peak(s) of the Lyα line profile, derived by fitting a Gaussian function to a small wavelength range ($\pm$0.6Å) centered around the visually identified position of the peak. For the four objects for which MIRRORB was used in the acquisition process, errors in the peak wavelength include the 0.1Å centering uncertainty. Hereafter we will use blue (red) peak, to identify the peak on the blue(red) side of the Lyα wavelength expected from Hα redshift. In Table **??** we report the total line flux, and the wavelength of the blue and red peak(s).

3.2. *Size measurement*

We use the COS images to measure the sizes of the galaxies in the NUV. Because of the complicated morphology of the starforming regions in many of the galaxies, we cannot fit a smooth profile to the UV light distribution (e.g., GALEX0332−2811A). We have therefore computed the radius of the circular aperture containing half of the total NUV flux. The centers used for the circular apertures are indicated with a cross in Figure 6. Because of the small aperture of the COS instrument, we use the GALEX NUV luminosity as an estimate of the total light of the galaxy. Before computing the aperture flux, we multiplied each NUV image by the COS aperture response map to account for the decreasing throughput as function of the spatial offset from the aperture center (**?**).

4. RESULTS

4.1. *UV-morphology*

Being sensitive to light between 1600 and 3100Å, the COS NUV channel images mostly probe the continuum coming from the hot young stars (Lyα is inside the covered wavelength range only for three of our galaxies, at $z > 0.31$). Figure 6 we show the HST NUV images of the 25 galaxies observed with COS, together with the position of the circular COS aperture (when it could be determined, see section 3). The galaxies show a variety of morphology in the NUV: in some objects (e.g., GALEX1417+5305 in Figure 6) the UV light is distributed smoothly over a large part of the COS aperture (i.e., diffuse objects), in others (e.g., GALEX1417+5228) the light is concentrated in a single compact star cluster (i.e., compact objects), while in others (e.g., GALEX1000+0157) the light is distributed in multiple clumps. The morphological classification is reported in Table **??**.

4.2. *Lyα profiles*

In Figure 3 we present the full COS spectra shifted into the rest-frame using the redhift measured from the Hα emission line. The spectra are boxcar smoothed using a box of 1Å, and are shifted in the vertical direction for clarity. The horizontal dashed lines show the zero flux level corresponding to each galaxy spectrum. Rest-frame UV spectra of starforming galaxies are characterized by strong absorption features from both the neutral and ionized interstellar medium and by P-Cygni profile lines typical of radiation driven winds in massive stars. In about half of the sample galaxies, we can identify the strongest rest-frame UV features. However, because of the low S/N of the spectra, an accurate analysis is not possible.

In Figure 3 we show the observed COS spectra centered on the galaxy systemic velocity derived using the Hα emission line. The spectra are shown after a 9 pixels ($\sim$0.1Å) boxcar average. In two galaxies (GALEX1418+5259 and GALEX0959+0149) the Lyα line is very faint, and it is detected only after a rather heavy boxcar smoothing ($\sim$ 0.7Å).

From the images shown in Figure 6 we cans In Figures **??** we show the profiles of the Lyα emission lines. The vertical dashed line shows the expected wavelength position of the Lyα based on optical-lines redshift measurements.

Depending on the S/N of the spectra the lines show a nice blue peak.

Figure **??** shows the

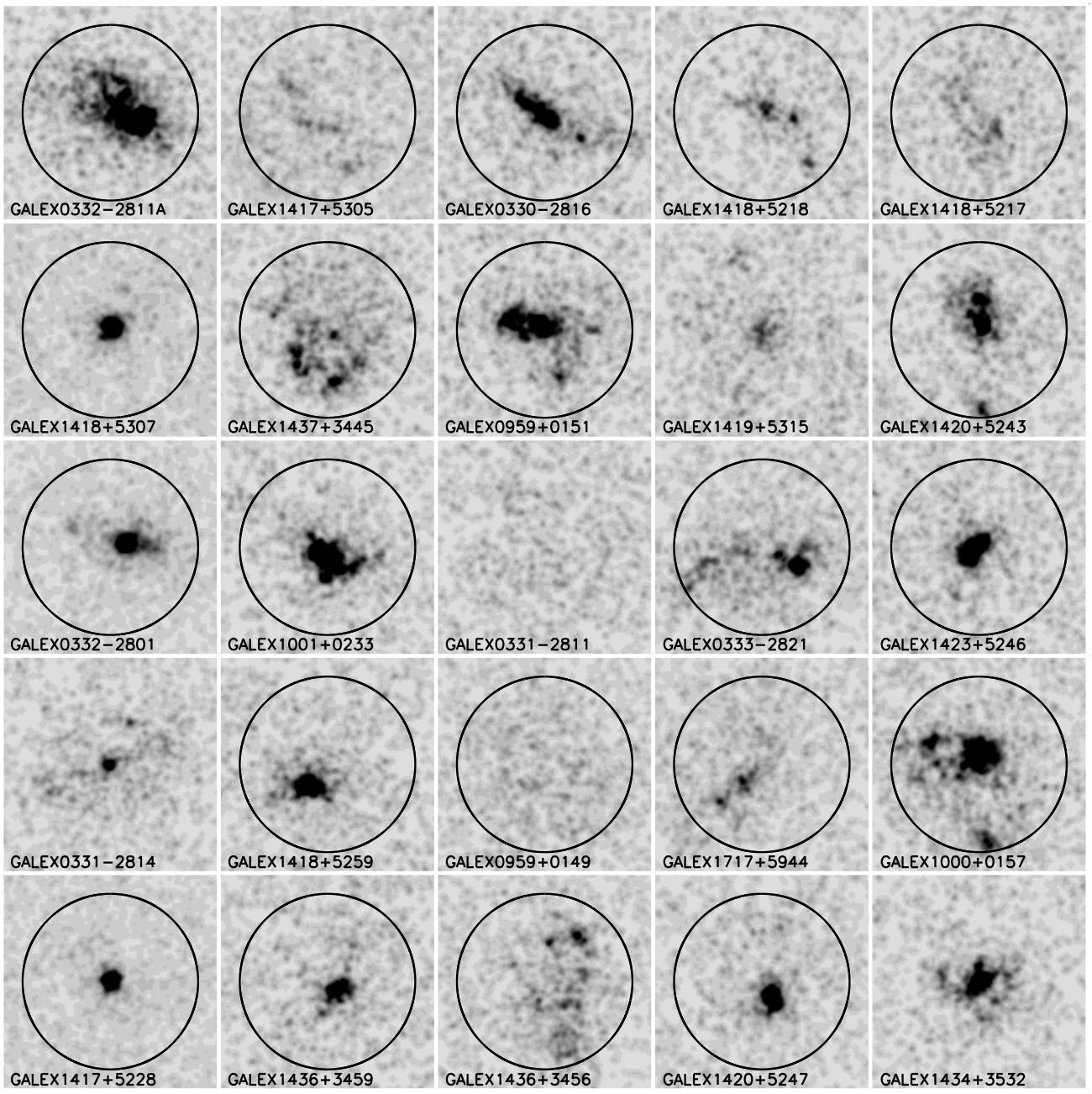

FIG. 1.— HST NUV images of the 25 sample galaxies observed with COS. The circle shows the position of the COS 2.″5 aperture on the object. For four galaxies the position could not be determined (see text for detail).

4.3. *Profile properties in various cases*

Let x be :

$$x = \frac{\nu - \nu_0}{\Delta\nu_D}; \qquad (1)$$

where $\nu_D = V_{th}/c\nu_)$ is the Doppler frequency width.

Homogeneous slab, monocromatic radiation What determines the shape of the output spectrum in this case are the temperature and the optical depth of the neutral medium. For a dust-free slab, the profile is double peaked and simmetric around $x = 0$. The peak frequency in this case (x_p) depends on T and τ_0 (the optical depth at the line center), with $x_p \sim \pm 0.88(a\tau_0)^1/3$. The more optically thick the medium is the more the peaks are separated.

In the presence of dust, the profile does not change much.

Expanding infalling halos The Lyα profiles resulting from a monochromatic source surroundes by an expanding/infalling shell of gas are perfectly symmetric to

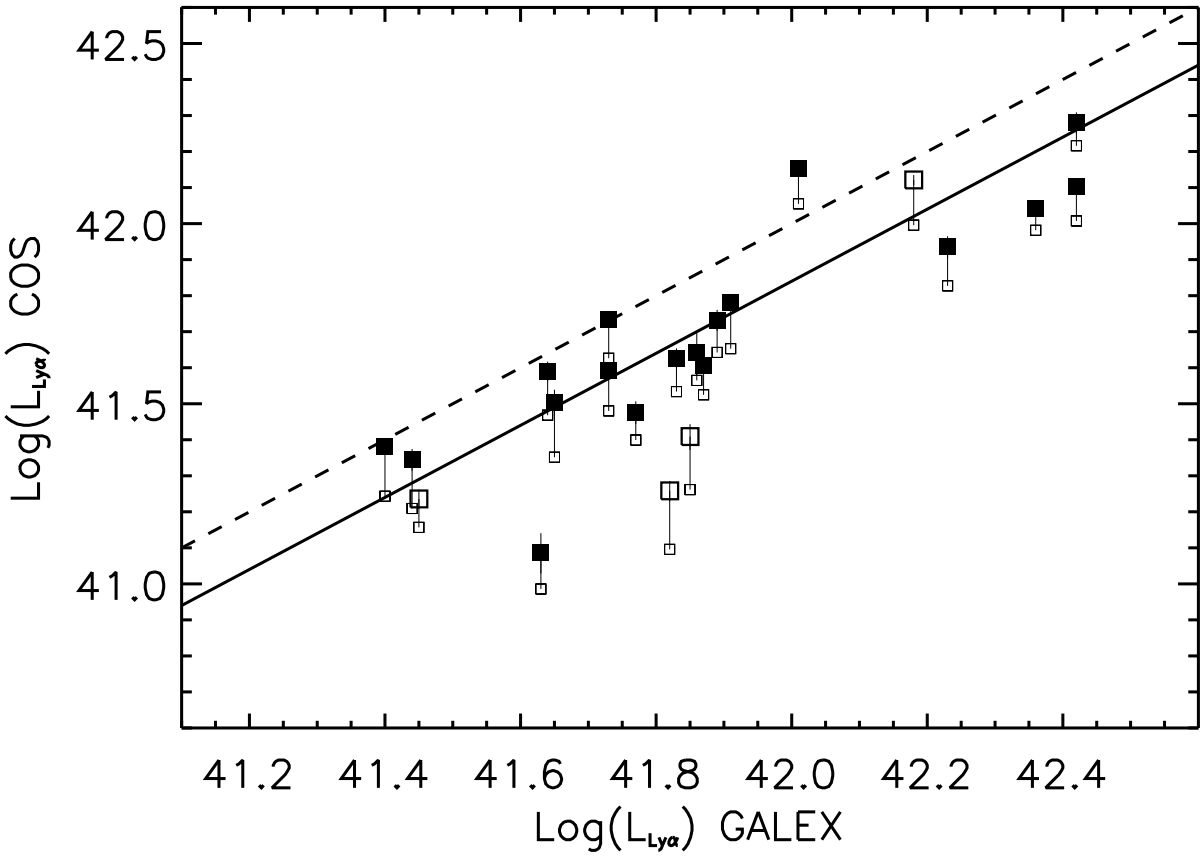

FIG. 2.— Comparison between the total Lyα flux measured in the COS aperture, and the Lyα flux measure from GALEX spectra. Large points have been corrected using the aperture correction estimated from the UV continuum. Open large squares indicate galaxies observed with MIRROR-B. After the aperture correction, approximately 30% of the Lyα flux is missed by the 2.″5 COS aperture, indicating that the Lyα emission is more extended than the continuum.

each other. Expanding halos present a red peak while infalling halos show a blue peak.

5. RADIATIVE DRIVEN STELLAR WINDS

Winds==¿ high density==¿ expnding material is opaque/optically thick to scattering in many atominc spectral-line transitions.

6. DUST GEOMETRY AND REDDENING

7. DISCUSSION

8. CONCLUSIONS

REFERENCES

Atek, H., Kunth, D., Hayes, M., Ostlin, G., Mas-Hesse, J. M. 2008, A&A, 488, 491
Atek, H., Kunth, D., Schaerer, D. et al. 2009, ArXive e-prints 0906.5349
Baldwin, J. A., Phillips, M. M., Terlevich, R. 1981, PASP, 93, 5
Bruzual, A. G. & Charlot, S. 1993, ApJ, 405, 538
Bruzual, G. & Charlot, S. 2003, MNRAS, 344, 1000
Caplan, J. & Deharveng, L. 1986, A&A, 155, 297
Cardelli, J. A., Clayton, G. C., Mathis, J. S. 1989, ApJ, 345, 245
Carter, B. J., Fabricant, D. G., Geller, M. J., Kurtz, M. J., & McLean, B. 2001, ApJ, 559,606
Charlot, S. & Fall, S. M. 1993, ApJ, 415, 580
Cowie, L.L., Barger, A.J., Hu, E.M., 2009, ArXive e-prints 0909.0031
Deharveng, J.-M., Small, T., Barlow, T. A. et al. 2008, ApJ, 680, 1072
Dijkstra, M., Haiman, Z., & Spaans, M. 2006, ApJ, 649, 14
Finkelstein, S. L., Rohads, J. E., Malhotra, S. et al. 2008, ApJ, 678, 655
Finkelstein, S. L., et al., 2009, ApJ, 700, 276
Finkelstein, S. L., et al., 2009, ApJ, ArXive e-prints 0906.4554
Giavalisco, M., Koratkar, A., & Calzetti, D. 1996, ApJ, 466, 831
Hansen, M. & Oh, S. P. 2006, MNRAS, 367, 979
Hayes, M. et al. 2007, MNRAS, 382, 1465
Kauffmann, G. et al. 2003, MNRAS, 341, 33
Kewley, L. J. et al. 2001, ApJ, 556, 121
Laursen, P. & Sommer-Larsen, J. 2007, ApJ, 657, L69
Mathis, J. S. 1972, ApJ, 176, 651
Miller, C. J. et al. 2003, ApJ, 597, 142
Natta, A. & Panagia, N. 1984, ApJ, 287, 228
Neufeld, D. A. 1990, ApJ, 350, 216
Neufeld, D. A. 1991, ApJ, 370, L85
Oke, J. B. & Gunn, J. E. 1982, PASP, 94, 586
Ostlin, G. et al. 2008, ArXiv e-prints
Panagia, N. & Ranieri, M. 1973a, A&A, 24, 219
Panagia, N. & Ranieri, M. 1973b, in Les Nebuleuses Planetaires, 275280
Pengelly, R. M. 1964, MNRAS, 127, 145
Valls-Gabaud, D. 1993, ApJ, 419, 7
Verhamme, A., Schaerer, D., & Maselli, A. 2006, A&A, 460, 397

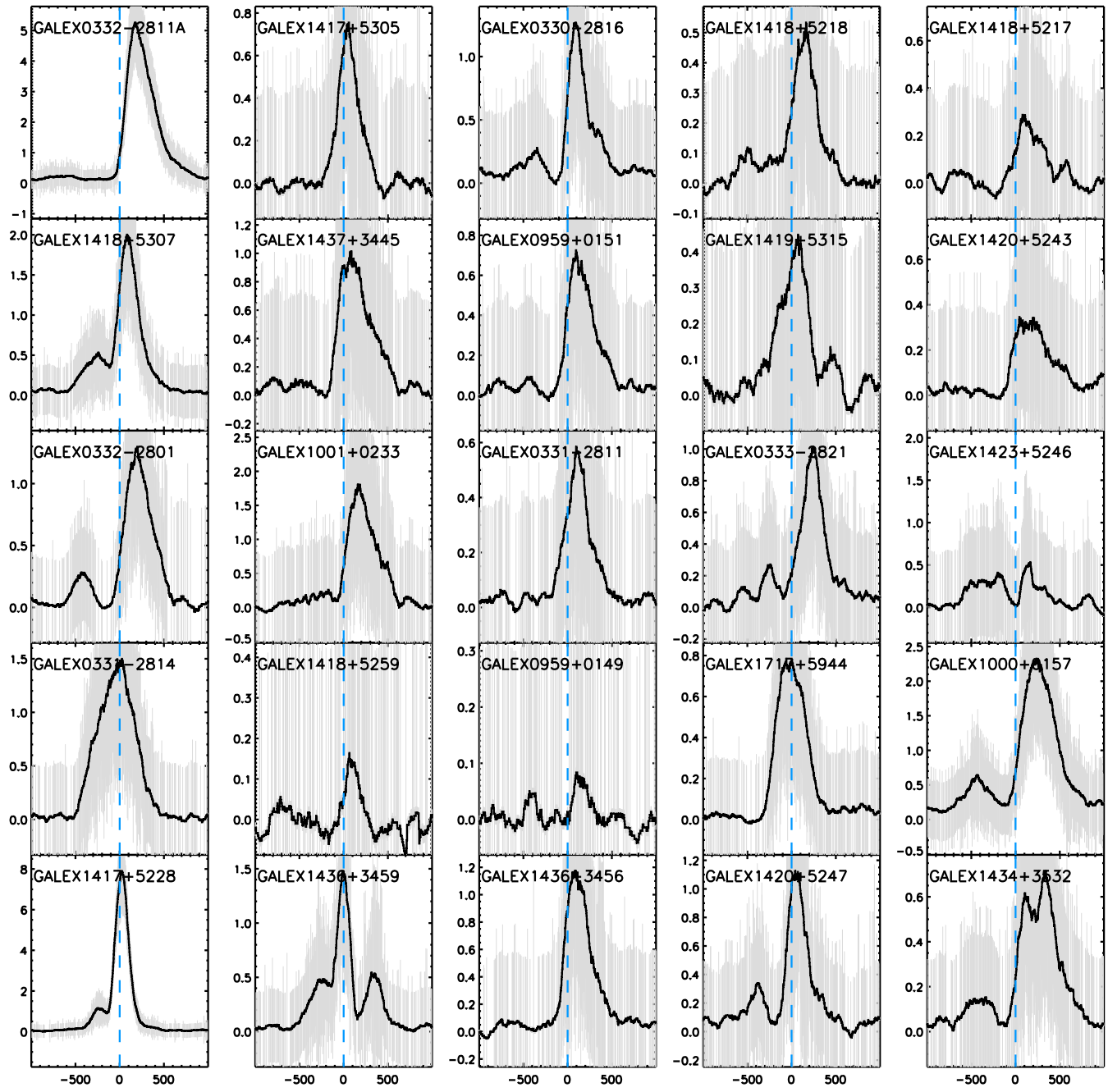

FIG. 3.— Rest-frame COS spectra of the 25 sample galaxies around the Lyα emission lines. The systemic velocity is determined from the nebular Hα line.

York, D. G. et al. 2000, AJ, 120, 1579

APPENDIX

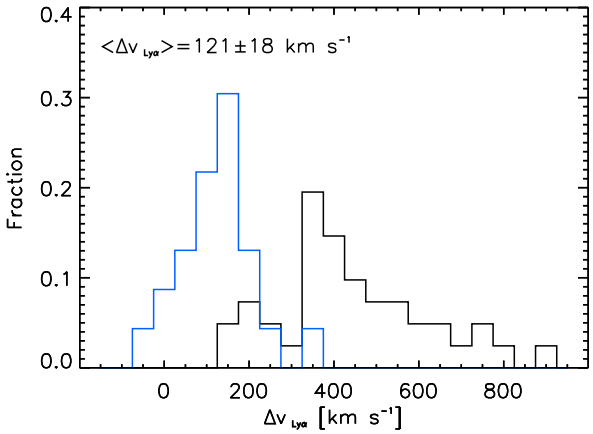

FIG. 4.— Histogram of the velocity shifts between the Lyα and Hα lines.

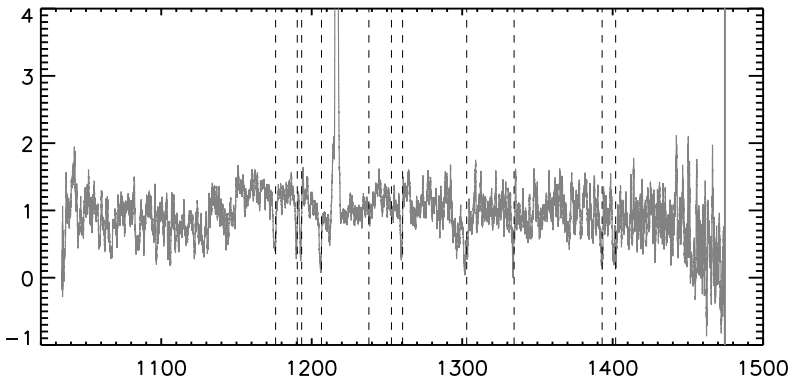

FIG. 5.— Composite spectrum from XXX galaxies.

TABLE 1
Lyα PROPERTIES

Galaxy	Lyα luminosity	λ_B	λ_R	Notes
	erg s^{-1}	Å		
GALEX1417+5228	1.38 ± 0.03 $\times 10^{42}$	1467.93 ± 0.01	1469.15 ± 0.01	
GALEX0331-2814[a]	1.30 ± 0.05 $\times 10^{42}$	···	1556.30 ± 0.10	
GALEX0332-2801	0.39 ± 0.02 $\times 10^{42}$	1475.82 ± 0.01	1478.90 ± 0.01	
GALEX1418+5307	0.53 ± 0.02 $\times 10^{42}$	1462.12 ± 0.01	1463.68 ± 0.03	
GALEX0332-2811A	1.06 ± 0.02 $\times 10^{42}$	···	1465.08 ± 0.01	
GALEX1436+3459	0.38 ± 0.02 $\times 10^{42}$	1473.83 ± 0.01	1474.98 ± 0.01	
GALEX1418+5259	0.04 ± 0.02 $\times 10^{42}$	···	···	
GALEX1001+0233	1.83 ± 0.14 $\times 10^{42}$	···	1682.10 ± 0.01	
GALEX1437+3445	0.83 ± 0.07 $\times 10^{42}$	···	1610.23 ± 0.01	
GALEX1417+5305	0.31 ± 0.03 $\times 10^{42}$	···	1541.07 ± 0.01	
GALEX1436+3456	0.59 ± 0.04 $\times 10^{42}$	···	1543.24 ± 0.01	
GALEX0959+0149	0.02 ± 0.00 $\times 10^{42}$	···	···	
GALEX0331-2811[a]	0.17 ± 0.01 $\times 10^{42}$	···	1474.29 ± 0.10	
GALEX0959+0151	0.29 ± 0.02 $\times 10^{42}$	···	1521.75 ± 0.01	
GALEX0330-2816	0.52 ± 0.04 $\times 10^{42}$	1555.92 ± 0.01	1558.40 ± 0.01	
GALEX1420+5247	0.40 ± 0.03 $\times 10^{42}$	1520.95 ± 0.01	1523.22 ± 0.01	
GALEX1717+5944	0.24 ± 0.01 $\times 10^{42}$	···	1453.92 ± 0.01	
GALEX0333-2821	0.37 ± 0.03 $\times 10^{42}$	1515.08 ± 0.01	1517.56 ± 0.01	
GALEX1419+5315[a]	0.25 ± 0.02 $\times 10^{42}$	1535.93 ± 0.10	1536.80 ± 0.10	
GALEX1418+5218	0.22 ± 0.02 $\times 10^{42}$	···	1507.02 ± 0.01	
GALEX1434+3532[a]	0.16 ± 0.01 $\times 10^{42}$	1453.15 ± 0.10	1454.12 ± 0.10	
GALEX1000+0157	1.23 ± 0.05 $\times 10^{42}$	1535.20 ± 0.01	1538.83 ± 0.03	
GALEX1423+5246	0.43 ± 0.07 $\times 10^{42}$	1632.31 ± 0.01	1634.03 ± 0.01	
GALEX1420+5243	0.11 ± 0.01 $\times 10^{42}$	···	1517.26 ± 0.01	
GALEX1418+5217	0.07 ± 0.01 $\times 10^{42}$	···	1508.37 ± 0.01	

[a] Galaxy observed with MIRRORB

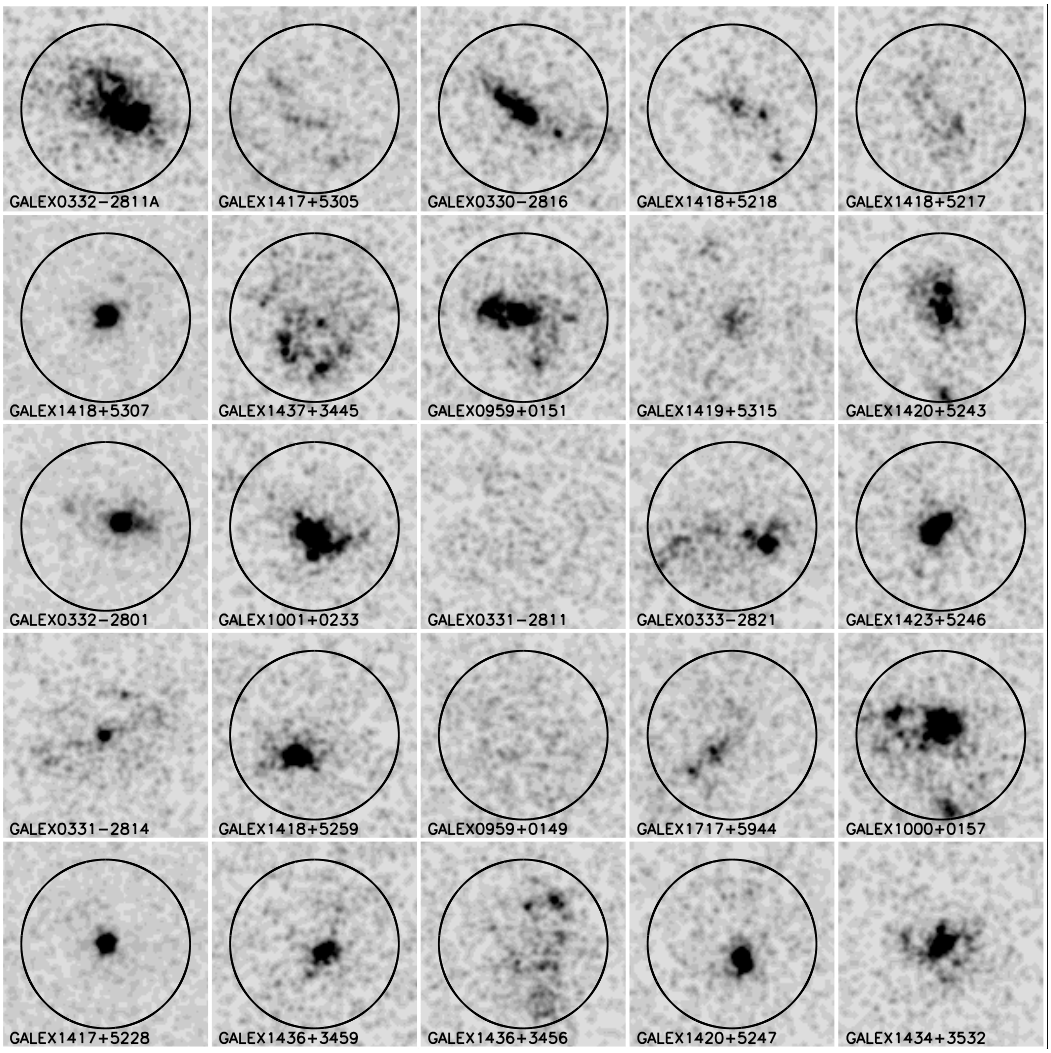

FIG. 6.— COS NUV images of the target galaxies. The circles show the position and size of the COS PSA aperture. For four galaxies an accurate position of the aperture could not be determined, and the aperture is not shown (see text for details).